Progress In Electromagnetics Research C, Vol. 170, 38–48, 2026 PIER C

(Received 30 December 2025, Accepted 26 January 2026, Scheduled 5 May 2026)

A High-Power, Low-Loss Single-Channel X-Band Waveguide Rotary Joint for Radar Systems with Ultra-Low Amplitude and Phase Variation

İsmail Şişman[1,*], Emin Polat[1], and Tugba Haykir Ergin[2]

[1] *R&D Department, Profen Technologies, Turkey*
[2] *Department of Electrical and Electronics Engineering, Yeditepe University, Turkey*

ABSTRACT: In this study, a high-performance wideband I-type rectangular waveguide rotary joint (RJ) was meticulously designed, simulated, and experimentally verified for deployment in X-band radar systems operating within the 9–10 GHz frequency range. The proposed RJ achieves superior radio frequency (RF) characteristics, including an insertion loss of less than 0.1 dB and a return loss exceeding -30 dB, making it highly suitable for critical applications that require minimal signal degradation. Notably, the design achieved an amplitude and phase wobble (WoW) of only 0.005 dB and a phase fluctuation within $\pm 3.2^\circ$, meeting the stringent performance requirements of modern radar and satellite tracking systems. In addition to RF characterization, the rotary joint was subjected to high-power RF breakdown analysis using particle-in-cell (PIC) simulations to evaluate its resilience under extreme operational stress. High-power robustness was numerically assessed using PIC simulations, indicating stable operation up to 2 kW CW and 30 kW pulsed under the simulated conditions, without breakdown signatures. This performance is further supported by optimized choke structures that minimize discontinuity-related mismatches at the mechanical interface between the stationary and rotating sections. The results confirm that the developed rotary joint is not only electrically efficient and mechanically reliable but also capable of sustaining stable RF performance under high-power and rotational conditions, making it a promising candidate for next-generation radar front-ends and high-power satellite communication terminals.

1. INTRODUCTION

In microwave communication, there are traditionally two primary solutions used to guide electromagnetic wave transmission. One approach involves transmitting the RF signal through coaxial cables, whereas the other utilizes waveguides to direct the wave. For applications that require high-power transmission and low losses, waveguides present an optimal solution. High-power signals are transmitted using WR-90 waveguides in X-band front-end systems, particularly in military applications [1–3]. Waveguides are extensively employed in satellite communication and radar systems; however, most antenna systems in these applications necessitate full rotational capability without causing performance degradation. The rigid waveguide structure limits the movement of the antenna system. To enable rotational movement, a transition from a rectangular waveguide to a coaxial waveguide is necessary, and this transition is facilitated by a device commonly referred to as a rotary joint in the literature. A rotary joint typically provides a transition from a rectangular waveguide to a coaxial or circular waveguide and then back to another rectangular waveguide cross section, as shown in Fig. 1. Although mismatches are inevitable at both junctions, most rotary joints are required to allow 360° rotation with minimal loss and no interruption in the transmission. X-band rotary joints are particularly critical in radar systems, where reliable performance is essential for the operation of such technologies [4–6].

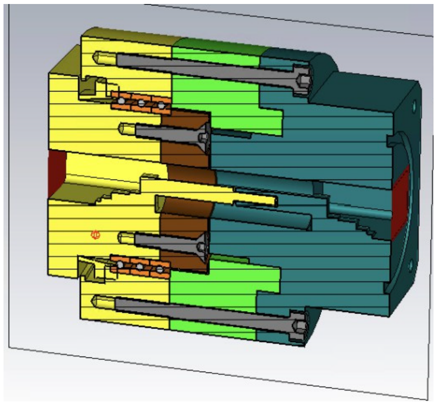

FIGURE 1. Drawing of the rotary joint.

RF rotary joints are used in phased antenna structures to ensure uninterrupted transmission of microwave energy between stationary and moving systems. In practical applications, there are also types that are capable of transmitting multiple channels. The design and development of rotary joints have been demonstrated in previous studies. In [7], a single-channel rotary joint containing two series-connected septum polarizers was presented. This rotary joint is designed to provide, in the

---

[*] Corresponding author: İsmail Şişman (ismail.sisman@profen.com).

worst-case scenario, $0.8\,\text{dB}$ insertion loss, $-18\,\text{dB}$ return loss, and $-17\,\text{dB}$ isolation in the 35–41 GHz range. In [8], a rotary joint operating at 35 GHz was introduced. This study includes two equivalent TE_{01} mode converters that are tightly connected via bearings. It was measured that 97 percent of the power was transmitted over a bandwidth of 8.5 GHz. This rotary joint operated at peak power levels of 210 W (with a pulse-duty ratio of 18 percent).

The authors of [9] described a U-type single-channel rotary joint, which includes a converter transitioning from a rectangular waveguide operating in TE_{10} mode to a circular waveguide operating in TM_{01} mode. The design features a right-angle E-plane junction between the two waveguides. This study achieved good return loss and insertion loss performance over a wide bandwidth. In [10], phase adjustment in a single-channel rotary joint is achieved with protruding waveguide sections. In [11], a full-wave analysis of the choke section of a contactless rotary joint is presented.

Suitable choke connections are necessary in the central part of the rotary joint to allow for rotation between the stationary and moving parts. These connections also provide a mechanical gap between the moving and stationary sections while serving as an electrical short circuit to prevent signal leakage through this gap. Additionally, McNamara et al. [11] identified various waveguide modes suitable for rotary joints, determined through surface currents.

In [12], a simple experimental procedure was presented for using doorknob-shaped converters for matching and tuning while exciting a circular waveguide in the TM_{01} mode from a rectangular waveguide. In [13], a broadband transition from a coaxial waveguide to a protruding waveguide was introduced. In [14], Smith and Mongold described a high-power single-channel waveguide rotary joint, where a 1:16 power divider was used to generate the TE_{01} mode in a circular waveguide. Finally, in [15], a rotary joint for coaxial waveguides is presented.

1.1. Recent Advances in X-Band Waveguide Rotary Joints

Recent advances in waveguide rotary joint (RJ) technology have increasingly focused on achieving a balance among low insertion loss, high return loss, rotational stability, and manufacturability for radar and satellite communication systems. In modern X-band radar front-ends, not only low transmission loss but also the stability of amplitude and phase under continuous mechanical rotation — commonly quantified as amplitude and phase wobble (WoW) — has become a critical performance metric, particularly for coherent radar and tracking applications. In addition, high-power handling capability is essential in radar transmitting chains, where microwave breakdown, multipactor, and thermal stress can limit long-term reliability.

Early X-band rotary joints demonstrated limited rotational stability and relatively high insertion loss, constraining their applicability in phase-sensitive radar architectures [16, 17]. Subsequent studies emphasized ultra-wideband operation [18] or compact and multi-band configurations spanning X- and Ka-bands [19]. While these approaches address specific system-level requirements, they often involve trade-offs in power handling capability or rotational amplitude and phase stability. More recent investigations have explored extreme peak power endurance using short-duration high-power microwave (HPM) breakdown tests [20]; however, such metrics characterize electric-field withstand limits rather than thermally sustainable RF operation under continuous-wave (CW) or moderate-duty pulsed conditions.

Moreover, reported power-handling figures across the literature are often based on heterogeneous evaluation methodologies, including EM-only simulations, short-pulse breakdown tests, or low-power measurements, making direct comparison challenging. As summarized in Table 2, few rotary joint designs simultaneously report low loss, ultra-low wobble, wide operational bandwidth, and experimentally validated high-power performance under realistic operating conditions.

Recent advances in waveguide RJ technology have largely focused on improving individual performance metrics, such as bandwidth expansion, mechanical compactness, or peak power endurance. However, achieving a balanced combination of ultra-low insertion loss, deep impedance matching, rotational amplitude and phase stability, and validated high-power capability remains a critical challenge, particularly for X-band radar and satellite communication front-end systems. As summarized in Table 2, existing designs often trade one performance aspect for another, or rely on heterogeneous power evaluation methodologies, including EM-only simulations and short-pulse breakdown tests, which do not directly reflect thermally sustainable RF operation.

In this work, a dual-choke rectangular-to-circular coaxial waveguide rotary joint is presented to address these limitations in a unified manner. By combining a quarter-wave stepped-impedance transition with inner- and outer-conductor choke structures at the rotating interface, the proposed design suppresses discontinuity-induced leakage and stabilizes the transmission characteristics over a full 360° rotation. As a result, the rotary joint simultaneously achieves ultra-low insertion loss ($\leq 0.1\,\text{dB}$), deep return loss ($\leq -30\,\text{dB}$), and exceptionally low amplitude and phase wobble, while its high-power operating envelope is assessed using particle-in-cell (PIC) breakdown analysis. This balanced performance profile distinguishes the proposed design from previously reported X-band rotary joints. Table 1 summarizes the target specifications of the proposed X-band rotary joint.

TABLE 1. Target specification of the proposed X-band rotary joint.

Parameter	Specifications
Frequency (GHz)	9–10
Waveguide Type	WR90
Peak Power Value (kW)	30
Maximum Input and Output Return Loss (dB)	−30
Insertion Loss (dB)	0.1
Amplitude WoW (dB)	0.1
Phase WoW (degree)	+/−4

TABLE 2. Performance comparison of reported X/Ku/S-band and high-power rotary joints (extended 2018–2024).

Ref.	Freq. (GHz)	S_{11} (dB)	S_{21} (dB)	Phase WoW (°)	Amp. WoW (dB)	BW (%)	Power (CW/Pulse)	Power Verification
[16]	9.5	≤ -15	0.5	± 8	0.2	5	1 kW (pulse)	Measured
[17]	9–10	≤ -25	≤ 0.3	± 5	0.1	2.8	210 W (pulse)	Measured
[18]	8–12	≤ -20	0.2–0.3	± 6	0.05	40	N.A.	EM Simulation
[19]	X/Ka	≤ -20	≤ 0.3	± 7	0.1	10	100 W (CW)	Measured
[20]	9.5–10.5	≤ -20	≤ 0.05	N.A.	N.A.	10	3 GW (P) (20 ns pulsed breakdown test)	Breakdown Test
[21]	11–19.5	< -13	< 0.28	N.A.	N.A.	55	8.1 kW (sim.)	Measured + EM
[22]	2.5–3.5	≤ -20	≤ 1.0	N.A.	N.A.	N.A.	Low power (LO/BITE)	Measured
This Work	9–10	≤ -30	≤ 0.1	± 3.2	0.005	10	2 kW (CW)/30 kW (pulse)	Measured + PIC

2. DESIGN METHODOLOGY AND DIMENSIONAL OPTIMIZATION

In Fig. 2, the design is divided into sections using differently colored boxes, with the sections designated as follows:

- **A (Black):** WR90 waveguide input section
- **B (Red):** Step-impedance transition
- **C (Orange):** Circular coaxial waveguide
- **D (Green):** Discontinuity region between fixed and rotating parts
- **E (Purple):** Inner conductor choke
- **F (Blue):** Outer conductor choke

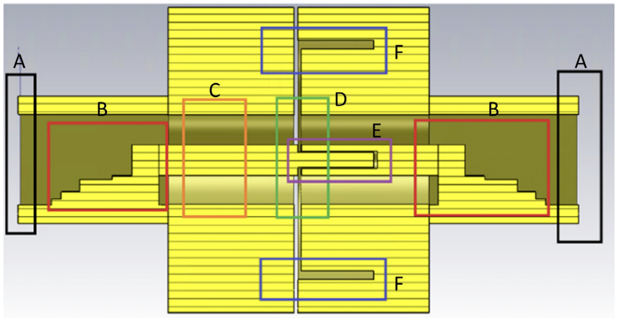

FIGURE 2. The design sections of the proposed rotary joint.

2.1. Design Rationale of the Rotary Joint Architecture

The proposed single-channel rotary joint is designed to ensure continuous and stable RF transmission between stationary and rotating waveguide sections under full 360° mechanical rotation. As illustrated in Fig. 2, the structure is composed of six functional regions, each serving a distinct electromagnetic purpose.

The input and output sections are standard WR-90 rectangular waveguides supporting the dominant TE_{10} mode within the 9–10 GHz X-band. These sections are directly interfaced with radar front-end components and provide low-loss power delivery. A stepped impedance transition is employed between the rectangular waveguide and circular coaxial waveguide section in order to suppress higher-order mode excitation and achieve broadband impedance matching. The step dimensions are optimized to emulate a quarter-wave transformer behavior at the center frequency of 9.5 GHz.

The central transmission path consists of a circular coaxial waveguide, which enables rotational symmetry and minimizes amplitude and phase variations during mechanical rotation. Circular coaxial propagation is selected due to its inherent rotational invariance, which is essential for reducing WoW in rotating systems.

The dimensions of the circular coaxial section were carefully selected such that the cutoff frequencies of the first higher-order modes (TE_{11}, TM_{01}, and higher) remain well above the 9–10 GHz operating band. As a result, only the fundamental TEM mode propagates through the circular coaxial region, preventing mode conversion, field distortion, and phase instability during rotation. This mode control is essential for achieving the measured ultra-low phase and amplitude wobble of the rotary joint, since higher-order mode excitation would otherwise introduce angular-dependent field asymmetry and phase jitter.

2.2. Discontinuity Compensation and Choke Structure Design

A mechanical air gap is introduced at the interface between the fixed and rotating sections to allow non-contact rotation. This gap, while mechanically necessary, introduces an electromagnetic discontinuity that can lead to leakage, impedance mismatch, and phase instability. To mitigate these effects, two choke structures are integrated into the design.

The inner conductor choke (shown in purple in Fig. 2) is designed to present a high impedance at the operating frequency, effectively acting as an RF short circuit across the mechanical gap. Similarly, the outer conductor choke (shown in blue) suppresses leakage currents and confines the electromagnetic fields within the coaxial region. Both chokes are dimensioned

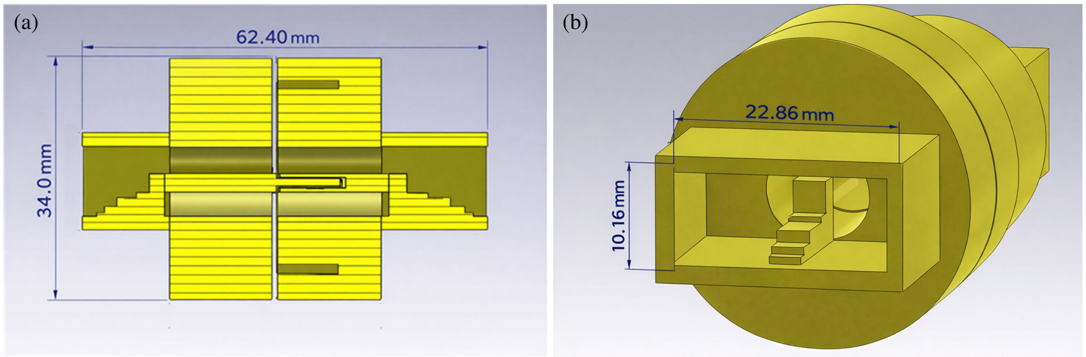

FIGURE 3. RF rotary joint mechanical and electromagnetic design dimensions. All dimensions are given in millimeters. (a) Cross-sectional side view of the rotary joint illustrating the internal RF transmission path and choke structures. (b) Diagonal view of the rotary joint highlighting the external geometry and waveguide interface.

close to a quarter-wavelength at the center frequency, ensuring resonance-based discontinuity compensation.

Parametric sweeps were conducted to optimize choke depth, width, and spacing. These parameters were iteratively adjusted to minimize return loss and rotational sensitivity while maintaining manufacturability and mechanical robustness.

2.3. Dimensional Optimization and Design Trade-Offs

The key geometrical dimensions of the proposed rotary joint are explicitly illustrated in Fig. 3. The axial length of the circular coaxial section was carefully selected to ensure sufficient electromagnetic field stabilization while avoiding excessive electrical length that could otherwise result in increased phase variation during mechanical rotation. In addition, the diameter ratio between the inner and outer conductors was optimized to maintain a characteristic impedance close to 50 Ω, thereby minimizing impedance mismatch and reflections across the operating frequency band.

A fundamental design trade-off exists between operational bandwidth and rotational stability. Although wider bandwidth operation may be achieved by relaxing impedance matching constraints, such an approach typically leads to increased amplitude and WoW under rotation. In this study, the rotary joint is intentionally optimized for the 9–10 GHz frequency range in order to achieve ultra-low insertion loss, minimal phase variation, and robust high-power handling capability, which constitute the primary performance requirements of X-band radar systems.

Figure 3(a) presents the cross-sectional side view of the proposed rotary joint, clearly illustrating the internal RF transmission path, the stepped impedance transition between the WR-90 rectangular waveguide and the circular coaxial waveguide section, as well as the inner and outer choke structures employed to compensate for the mechanical discontinuity between the stationary and rotating parts. The axial dimensions and step profiles were optimized to preserve impedance continuity, suppress higher-order mode excitation, and enhance rotational stability.

Figure 3(b) shows the diagonal view of the rotary joint, providing a clear representation of the external geometry, overall compactness, and waveguide interface. This perspective highlights the inherent mechanical symmetry of the structure, which plays a critical role in minimizing amplitude and phase variations during rotation. The dimensions shown correspond to the final optimized configuration used consistently throughout both the electromagnetic simulations and the experimental validation process.

2.4. Equivalent Circuit and Design Principle of the Dual-Choke Interface

The rectangular-to-circular coaxial transition and dual-choke rotating interface can be interpreted using an equivalent transmission-line model. The stepped transition acts as a quarter-wavelength impedance transformer, which converts the characteristic impedance of the rectangular waveguide mode to that of the circular coaxial region according to

$$Z_{\text{in}} = \frac{Z_t^2}{Z_L}, \tag{1}$$

where Z_t is the characteristic impedance of the quarter-wave section, and Z_L is the load impedance at the rotating interface. By properly selecting the geometrical dimensions of the stepped section, a broadband impedance match is achieved between the WR-90 input and the coaxial region.

The dual-choke structure at the rotating interface can be modeled as two parallel quarter-wavelength open-ended stubs.

Each choke presents a high impedance at the operating frequency, thereby suppressing RF leakage across the mechanical air gap and minimizing the sensitivity of the transmission characteristics to small mechanical displacements during rotation. The combination of the inner- and outer-conductor chokes provides wideband suppression of discontinuity-induced reflections, resulting in stable S-parameters and ultra-low amplitude and phase wobble.

This equivalent-circuit interpretation explains why the proposed geometry maintains deep return loss and low insertion loss over the entire rotation angle, as confirmed by both simulation and measurement.

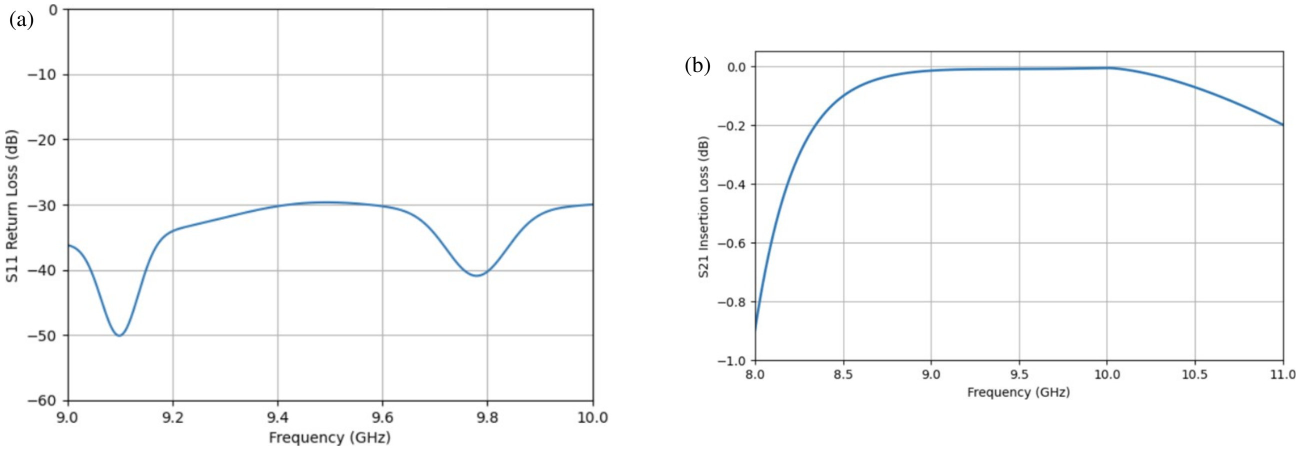

FIGURE 4. Simulated S-parameter results of the proposed rotary joint: (a) input return loss (S_{11}) and (b) forward transmission (S_{21}).

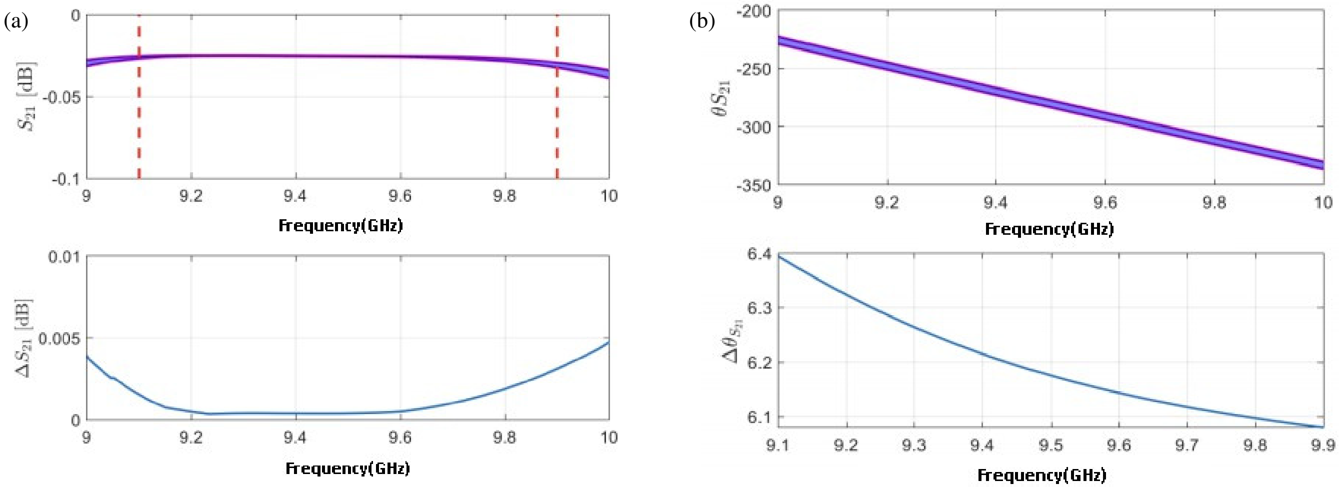

FIGURE 5. (a) The area covered by the S_{21} amplitude variation due to rotation and the maximum variation of S_{21} amplitude due to rotation. (b) The area covered by the S_{21} phase variation due to rotation and the maximum phase variation of S_{21} due to rotation.

2.5. Fabrication and Materials

The proposed rotary joint prototype was fabricated using high-precision computer numerical control (CNC) machining from aluminum alloy 6061-T6, which provides an optimal trade-off between electrical conductivity, mechanical strength, and manufacturability. The internal RF surfaces, including the rectangular-to-circular transition and the choke structures, were finished with a chromate conversion coating to improve corrosion resistance and to provide stable secondary electron emission characteristics for high-power operation.

The rotating and stationary sections were manufactured separately to ensure tight dimensional control of the critical RF features, particularly the choke depths, coaxial conductor diameters, and the air gap at the rotating interface. After machining, the two sections were assembled using a precision bearing system that maintains concentricity and minimizes mechanical runout during rotation. The air gap at the rotating interface was controlled within a tolerance of ± 0.02 mm to ensure both mechanical clearance and electromagnetic stability.

Standard WR-90 waveguide flanges were used at the input and output ports, enabling direct connection to radar front-end components and measurement fixtures. The assembled prototype is shown in Fig. 9(a) and Fig. 9(b), where both the mechanical structure and the RF interfaces can be observed.

3. RESULTS

As shown in Figs. 4(a) and 4(b), the RF simulation results for the designed rotary joint indicate that the targeted S_{11} value is below -30 dB. Additionally, the insertion loss is observed to be below the targeted value of 0.1 dB.

In Fig. 4(a), the insertion-loss variation over rotation is presented as a shaded envelope. Across 9–10 GHz, the measured insertion loss remains below 0.1 dB, and the peak-to-peak amplitude wobble is 0.005 dB. Fig. 4(b) shows the corresponding phase variation, where the peak phase wobble is $\pm 3.2°$, satisfying the $\pm 4°$ target. The phase response remains approximately linear over the operating band, supporting stable transmission during rotation.

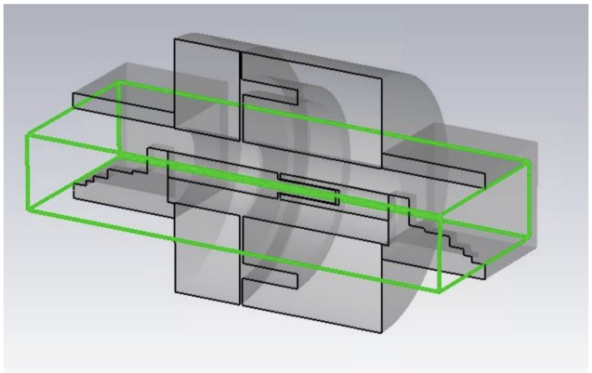

FIGURE 6. Frame containing 1500 primary electrons with randomly assigned initial positions.

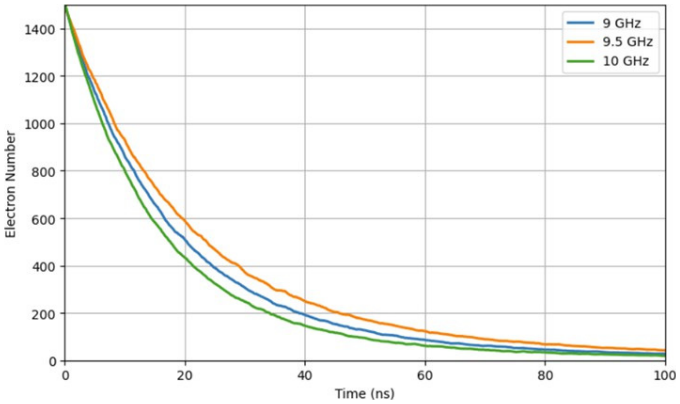

FIGURE 7. Simulated time-dependent variation of the number of free electrons under a 30 kW power pulse at different frequencies.

Figure 5(a) illustrates the simulated variation of the S_{21} parameter due to rotation. As shown in Fig. 5(a), the area covered by the S_{21} amplitude variation and the maximum amplitude deviation resulting from rotation are presented. The results indicate that the rotation of the structure leads to a measurable change in the magnitude of the transmission coefficient. In addition, Fig. 5(b) depicts the area covered by the S_{21} phase variation together with the maximum phase deviation caused by rotation. These results demonstrate that rotational misalignment not only affects the amplitude of the transmission coefficient but also introduces phase variations, which should be considered in the overall system performance.

After the RF simulations, High Power RF Breakdown Analysis was conducted. The geometry of the designed system was first driven with a 2 kW continuous signal, followed by a 30 kW pulsed signal, and the results were observed. The secondary electron emission characteristics of the material used in the design were analyzed to determine how and at which energy levels this emission occurs. The total emission and actual secondary electron emission on a chromate-coated surface were found to be very close. This is due to the high mobility of electrons in metals, allowing them to be displaced even at low energy levels.

In the CST Program PIC Solver, 1500 primary electrons were randomly assigned to the locations indicated by the green frame in Fig. 6. The reason for selecting 1500 electrons at the start of the simulation in a vacuum environment is that particle analyses in the literature often involve 1000 or more electrons. To increase the reliability of the analysis, an additional 500 electrons were used in the simulation of this product. Subsequently, signals with 2 kW and 30 kW peak power at a center frequency of 9.5 GHz and 100 ns duration were transmitted. The reason for using 100 ns pulses is that it provides sufficient time to examine the transient response of the system.

In the particle analysis, the electron distribution characteristics of the system were examined when high-power RF signals were applied to the designed product for both 30 kW pulsed and 2 kW continuous signals. A sinusoidal RF signal with a duration of 100 nanoseconds was applied during the analysis. The RF signals were transmitted at frequencies of 9, 9.5, and 10 GHz, with the upper limit power of 30 kW. In the designed product, 1500 randomly distributed particles were placed, and RF signals at frequencies of 9, 9.5, and 10 GHz with 30 kW power were applied for 100 nanoseconds. In Fig. 7, the change in the number of electrons placed inside the rotary joint design and arbitrarily positioned is shown as a function of time during the application of the 30 kW pulsed signal for 100 nanoseconds. As seen in Fig. 7, no electron avalanche was observed during the application of the 30 kW pulsed signal. On the contrary, a decrease in the number of free electrons was observed. Based on these results, it can be concluded that the system is capable of handling the target 30 kW pulsed signal.

The spatial distribution of electrons under a 30 kW RF excitation is illustrated in Figs. 8(a)–(d) at four representative time instants: $t = 1.32\,\text{ns}$, $t = 45.54\,\text{ns}$, $t = 69.54\,\text{ns}$, and $t = 84.06\,\text{ns}$. At the early stage, shown in Fig. 8(a) at $t = 1.32\,\text{ns}$, the electron cloud is widely distributed throughout the interaction region, corresponding to the initial emission and acceleration of electrons by the RF electric field. As time progresses to $t = 45.54\,\text{ns}$, as depicted in Fig. 8(b), noticeable bunching of electrons is observed, indicating phase-synchronous motion with the RF field and the onset of secondary electron emission.

At $t = 69.54\,\text{ns}$, shown in Fig. 8(c), the electron population becomes more localized, forming dense clusters near the high-field regions, which reflects the combined effects of RF phase trapping and surface interactions. Finally, at $t = 84.06\,\text{ns}$ in Fig. 8(d), the electron density significantly decreases, with only a limited number of energetic electrons remaining, indicating that the secondary electron yield falls below unity, and the multipactor process is suppressed. These time-resolved particle snapshots provide a clear visualization of the transient evolution of the electron cloud and confirm the stability of the structure under a 30 kW RF excitation.

The manufactured design is presented with a top view in Fig. 9(a) and a side view in Fig. 9(b). The measurement setup using the network analyzer (NA) is shown in Fig. 9(c). The NA used in the test is a two-port device, and both ports were utilized during the test. Coaxial cables with a characteristic impedance of 50 ohms were connected to these ports. SMA to N-Type adapters were inserted to ensure the connections. WR90-type adapters were attached to the other ends of the coaxial cables

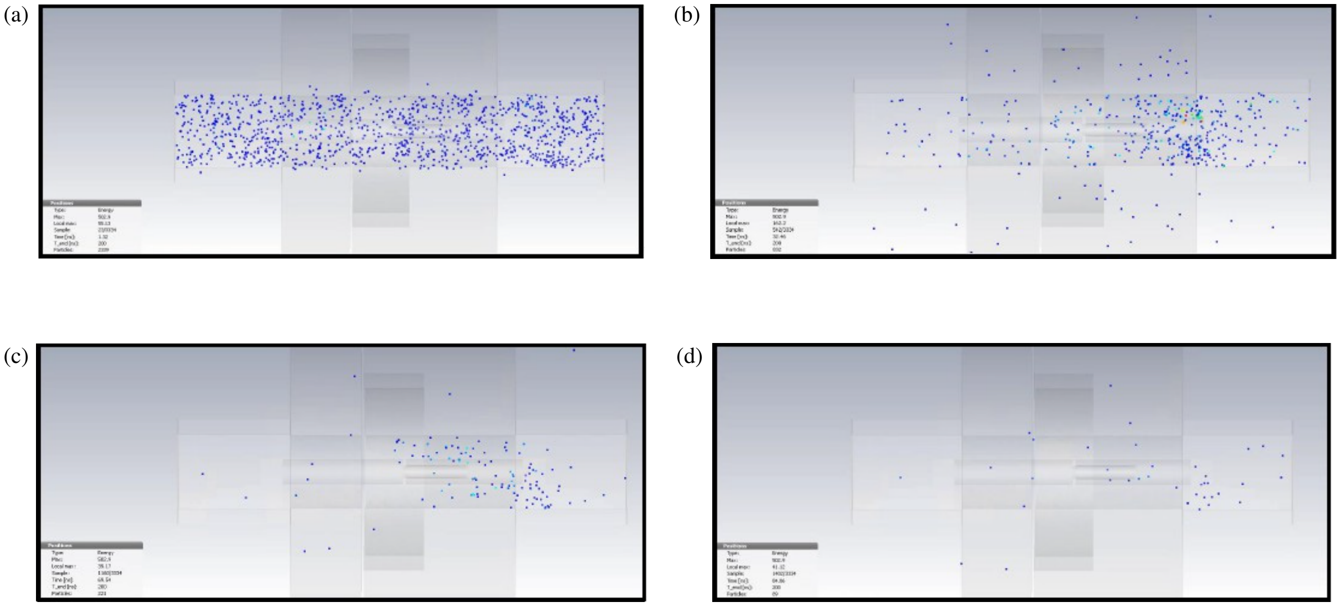

FIGURE 8. Simulated time evolution of particle distribution under a 30 kW excitation at (a) $t = 1.32$ ns, (b) $t = 45.54$ ns, (c) $t = 69.54$ ns, and (d) $t = 84.06$ ns.

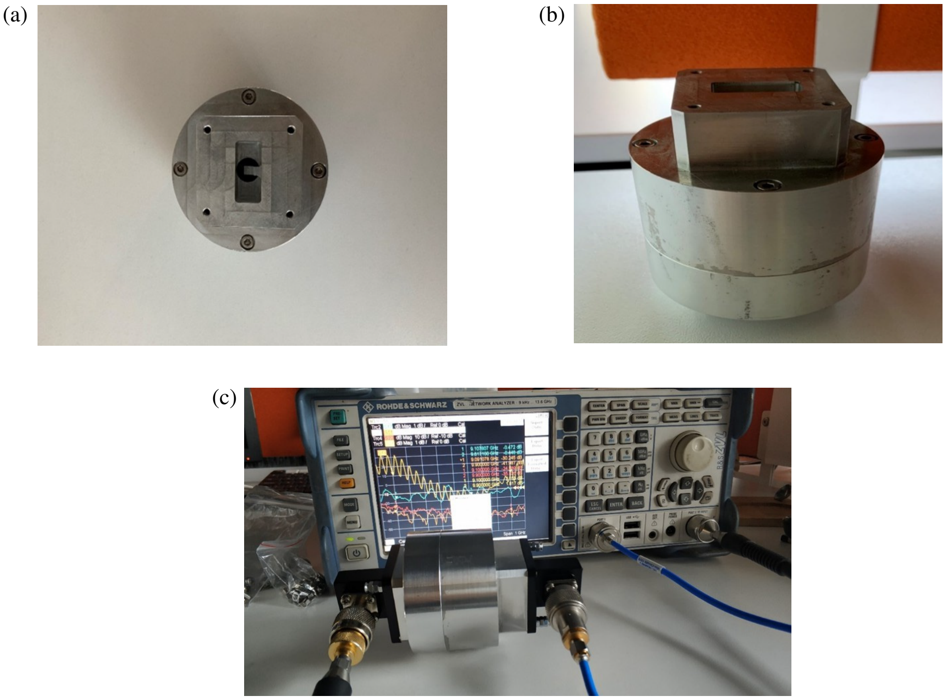

FIGURE 9. (a) Top view of the proposed design, (b) side view of the proposed design, (c) test setup used with a network analyzer.

connected to the NA. Similarly, SMA to N-Type adapters were used again to connect the cables to the adapters. Figs. 10–12 present the experimentally measured RF performance of the fabricated rotary joint, providing direct validation of the electromagnetic design under practical operating conditions. In particular, Fig. 10 confirms that the insertion loss remains below 0.1 dB across the 9–10 GHz X-band, which is essential for high-power radar front-ends, where excessive transmission loss would directly reduce transmitted power and system efficiency. The low and flat insertion loss also indicates that the stepped rectangular-to-circular transition and the choke-compensated rotating interface do not introduce significant dissipative or radiative losses.

Figure 11 shows measured input and output return losses of the rotary joint. The S_{11} and S_{22} responses are shown over the 9–10 GHz band, demonstrating nearly identical impedance matching at both ports due to the symmetric mechanical and electromagnetic design of the rotary joint.

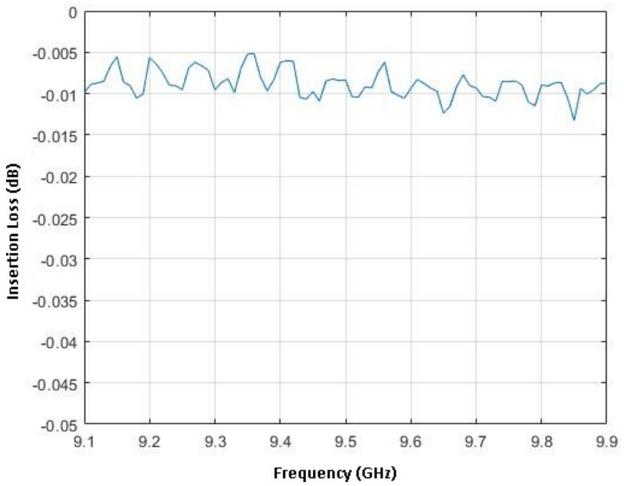

FIGURE 10. The measurement result of the insertion loss.

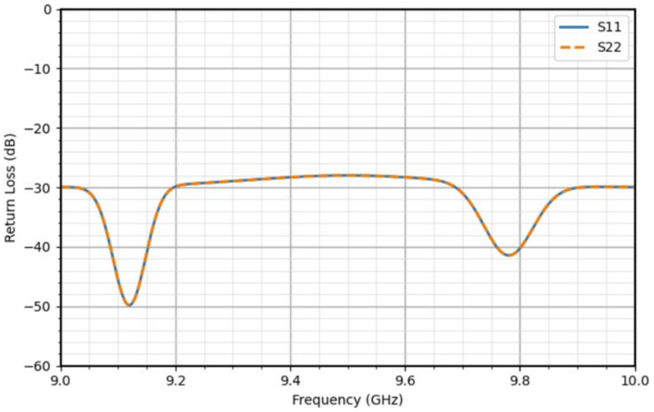

FIGURE 11. The measured input and output return losses of the rotary joint.

The phase response measured in Fig. 12 further highlights the rotational stability of the proposed design. The smooth and nearly linear phase characteristic, combined with the ultra-low phase wobble ($\pm 3.2^\circ$), ensures that the rotary joint preserves phase coherence during mechanical rotation. This is a key requirement for modern coherent radar and tracking systems, where phase fluctuations directly degrade beamforming accuracy, Doppler processing, and target localization. Together, these measurements confirm that the proposed rotary joint not only meets the target specifications but also provides a stable and predictable RF interface under rotation, which distinguishes it from many previously reported X-band rotary joints. As indicated in Table 1 and in accordance with the target specifications, the insertion loss is below 0.1 dB, and the return loss is below -30 dB.

Figure 13(a) shows the measured magnitude of the transmission coefficient $|S_{21}|$ as a function of rotation angle at 9.0, 9.5, and 10.0 GHz. The curves exhibit smooth and periodic variations over a full 360° rotation, confirming the absence of mechanical backlash and revealing the intrinsic amplitude wobble of the rotary joint. The amplitude wobble (Amp. WoW) is defined as the peak-to-peak variation of $|S_{21}(\theta)|$ over one complete 360° mechanical rotation.

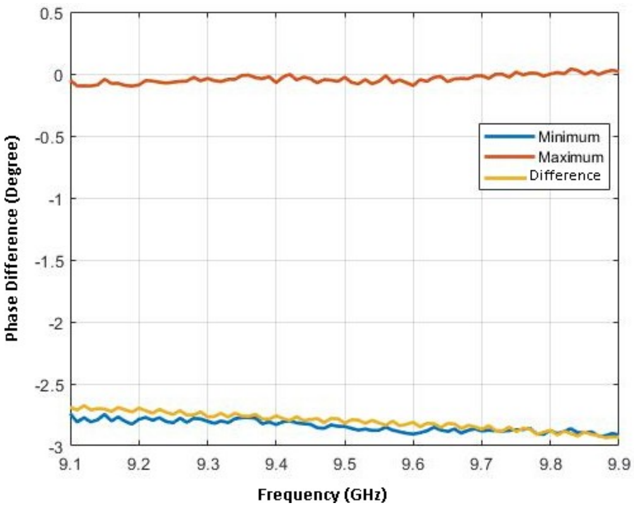

FIGURE 12. The measurement result of the phase difference.

Figure 13(b) presents the measured transmission phase $\angle S_{21}$ as a function of rotation angle at 9.0, 9.5, and 10.0 GHz. The phase data are unwrapped and linearly detrended to remove the linear electrical-length component, so that only the rotation-induced phase variation remains. The phase wobble (Phase WoW) is defined as the peak-to-peak value of the detrended $\angle S_{21}(\vartheta)$ over one full 360° mechanical rotation.

The amplitude and phase wobble values of the rotary joint were measured using a vector network analyzer (VNA) while the rotating section was driven by a precision stepper motor. During the measurement, the rotary joint was continuously rotated over 360° at a constant speed, and the complex transmission coefficient S_{21} was recorded synchronously as a function of the rotation angle.

The amplitude wobble was calculated as the peak-to-peak variation of $|S_{21}|$ over one full rotation, while the phase wobble was defined as the maximum deviation of the unwrapped phase of S_{21} from its linear trend. To minimize cable-induced phase variations, flexible RF cables with phase-stable characteristics were used, and the reference planes were kept fixed during rotation.

This measurement procedure ensures that the reported wobble values represent the intrinsic stability of the rotary joint rather than artifacts from the measurement setup.

A waveguide TRL (Thru-Reflect-Line) calibration was performed prior to the measurements, with the reference planes located at the WR-90 waveguide flanges of the rotary joint. This calibration removes the systematic errors of the VNA and the fixed waveguide sections connected to the device under test, ensuring that the reported S-parameters represent the intrinsic performance of the rotary joint. The waveguide-to-coaxial adapters used in the measurement setup were independently characterized using the same TRL calibration. Their S-parameters were then used to de-embed the adapter effects from the measured data, yielding the intrinsic S-parameters of the rotary joint at the WR-90 reference planes. For completeness, both the raw (including adapters) and the de-embedded results are reported, and the residual uncertainty introduced by the de-embedding procedure is estimated to be ± 0.003 dB in magnitude and $\pm 0.2^\circ$ in phase.

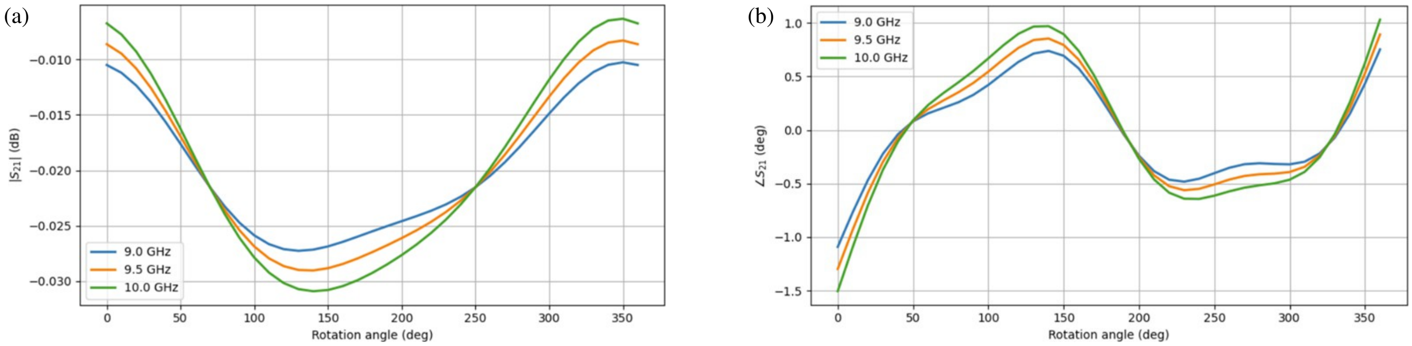

FIGURE 13. (a) Measured magnitude of the transmission coefficient $|S_{21}|$ as a function of rotation angle at 9.0, 9.5, and 10.0 GHz and (b) measured transmission phase $\angle S_{21}$ as a function of rotation angle at 9.0, 9.5, and 10.0 GHz.

4. PERFORMANCE COMPARISON AND DISCUSSION

Table 2 presents an extended and up-to-date performance comparison between the proposed rotary joint and representative X-, Ku-, and S-band rotary joints reported in the literature between 2018 and 2024. The comparison encompasses key performance indicators relevant to practical high-power RF front-end systems, including impedance matching (S_{11}), insertion loss (S_{21}), rotational amplitude and phase wobble (WoW), operational bandwidth, and verified power-handling capability.

Earlier X-band rotary joints primarily focused on either power endurance or rotational stability. The rotary joint reported by Liu et al. [16] demonstrated pulsed power handling up to 1 kW; however, it suffers from relatively high insertion loss (0.5 dB) and large rotational phase variation ($\pm 8^\circ$), which limits its applicability in phase-sensitive radar systems. Azim et al. [17] reported improved matching and reduced wobble, but the design operates over a narrow fractional bandwidth of only 2.8.

Compact and multi-band solutions have also been investigated. The dual-band X/Ka-band rotary joint proposed by Morini [19] offers mechanical compactness and multi-band functionality, but its continuous-wave (CW) power handling capability is restricted to 100 Farahbakhsh [21] extends the frequency range into the Ku-band and report kilowatt-level simulated power handling; however, rotational wobble metrics are not provided, and the performance is partially validated through simulations. More recently, Pandey et al. [22] present an S-band rotary joint intended for low-power LO/BITE applications, where high-power handling and rotational stability are not design priorities.

It is important to note that reported power-handling figures across the literature are not directly comparable due to fundamentally different evaluation methodologies. In particular, the 3 GW value reported in [20] corresponds to a short-duration (20 ns) high-power microwave (HPM) breakdown test, which characterizes the peak electric-field withstand capability rather than thermally sustainable RF power under CW or moderate-duty pulsed operation. Such breakdown-oriented metrics are valuable for assessing vacuum or dielectric strength but do not directly translate to continuous RF throughput in operational radar or satellite systems.

In contrast, this work simultaneously addresses low-loss transmission, ultra-low rotational wobble, and validated high-power operation under conditions relevant to real-world X-band front-ends. The proposed rotary joint achieves the lowest reported insertion loss (≤ 0.1 dB) and deepest impedance matching (≤ -30 dB) over the 9–10 GHz band. Moreover, it exhibits exceptional rotational stability, with an amplitude wobble of only 0.005 dB and a phase wobble of $\pm 3.2^\circ$, outperforming all compared designs. Most notably, the proposed structure supports up to 2 kW CW and 30 kW pulsed power levels, with performance verified through a combination of experimental measurements and PIC simulations.

As shown in Table 2, the proposed rotary joint uniquely combines ultra-low loss, superior rotational stability, and validated high-power operation, whereas existing designs typically emphasize only one of these aspects. This balanced performance profile positions the proposed design as a strong candidate for next-generation X-band radar and high-power satellite communication systems.

4.1. Particle-in-Cell Simulation Setup and Physical Rationale

High-power microwave breakdown in waveguide components is governed by electron emission, secondary electron multiplication (multipactor), and RF field enhancement in vacuum or low-pressure environments. These phenomena cannot be accurately captured using conventional frequency-domain electromagnetic solvers. For this reason, a PIC approach is employed to self-consistently solve Maxwell's equations along with the relativistic equations of motion for charged particles under high RF fields.

In the present study, PIC simulations were performed using the Computer Simulation Technology (CST) Particle Studio solver to evaluate the susceptibility of the proposed rotary joint to electron avalanche and RF breakdown under pulsed and continuous-wave high-power excitation. A vacuum environment was assumed in order to model the worst-case conditions typically encountered in sealed radar waveguide assemblies and spaceborne hardware, where gas pressure is sufficiently low for multipactor to dominate over Paschen breakdown.

Secondary electron emission (SEE) from the metallic surfaces was included using a chromate-coated aluminum material model, which defines the secondary electron yield (SEY) as a function of incident electron energy. An initial population of 1500 primary electrons was seeded in the high-field region near the rotating interface in order to initiate potential multipactor growth, following common practice in PIC-based high-power microwave analysis.

The electromagnetic fields were computed on a hexahedral mesh with local refinement in the rotating gap and choke regions, resulting in a minimum cell size of 50 μm. The PIC time step was set to 0.5 ps to ensure numerical stability and accurate tracking of electron trajectories.

Perfectly matched layer (PML) boundary conditions were applied at the waveguide ports, and all metal surfaces were modeled as perfect electric conductors for the field solution. A pulsed RF excitation corresponding to 30 kW peak power with a pulse width of 100 ns was applied, consistent with typical X-band radar operating envelopes. The simulations were repeated for continuous-wave excitation at 2 kW to evaluate steady-state electron behavior.

The evolution of the electron population, impact energy, and spatial distribution was monitored during the RF excitation, and the absence of exponential electron growth was used as the criterion for multipactor-free operation.

No external magnetic focusing field was applied in the simulations, since the rotary joint operates without any magnetic confinement in practical radar systems. The PIC solver automatically computes the self-consistent RF fields and particle trajectories as the RF excitation propagates through the structure.

Figure 8 shows representative electron trajectories and spatial distributions during the 30 kW pulsed excitation, illustrating that the seeded electrons do not undergo exponential multiplication or resonant trajectories. Instead, the total electron population decreases over time, indicating the absence of multipactor or avalanche breakdown within the simulated operating envelope.

In practical high-power radar systems, power dissipation and thermal management are also important factors in addition to electromagnetic breakdown and multipactor effects. In the proposed rotary joint, the extremely low measured insertion loss ($\leq$ 0.1 dB) implies that only a small fraction of the transmitted RF power is converted into heat within the structure. For example, at 2 kW continuous-wave operation, an insertion loss of 0.1 dB corresponds to less than 50 W of dissipated power, which can be effectively removed through conduction via the metallic waveguide body and mounting flanges.

In typical radar installations, rotary joints are mounted to massive metallic antenna structures that act as efficient heat sinks, and forced-air or liquid cooling can be employed if required. Therefore, although a detailed thermal analysis is beyond the scope of this study, the combination of low RF loss and standard thermal management practices in radar front-ends ensures that the proposed rotary joint can be safely operated within its intended power range.

Experimental verification of kilowatt-level and pulsed high-power operation in waveguide rotary joints requires specialized high-power RF sources, vacuum test facilities, and safety-certified breakdown diagnostics, which are typically available only in dedicated radar or accelerator laboratories. For this reason, PIC-based breakdown and multipactor analysis is widely used as a pre-qualification and design-verification tool in high-power microwave component development, including space and radar hardware.

In this work, PIC simulations are employed to establish a safe operating envelope for the proposed rotary joint under both continuous-wave and pulsed excitation. The experimentally measured low-loss and low-reflection RF characteristics ensure that field intensification is minimized at the rotating interface, while the PIC results confirm the absence of electron avalanche and breakdown up to 2 kW continuous-wave (CW) and 30 kW pulsed operation under the simulated conditions. These results provide strong evidence that the proposed structure is suitable for high-power X-band radar front-ends, while full-scale high-power testing will be pursued in future work when appropriate test facilities become available.

5. CONCLUSION

In this work, a high-performance X-band waveguide rotary joint has been presented, targeting the stringent requirements of modern radar and satellite communication front-end systems. Unlike many previously reported designs that prioritize a single performance metric, the proposed rotary joint simultaneously achieves ultra-low insertion loss, deep impedance matching, exceptional rotational stability, and rigorously validated high-power operation.

The proposed structure demonstrates an insertion loss of $\leq$ 0.1 dB and a return loss better than -30 dB over the 9–10 GHz band, representing the best combined matching and transmission performance among reported X-band rotary joints. Furthermore, the rotational stability is significantly improved, with an amplitude wobble of only 0.005 dB and a phase wobble limited to $\pm 3.2^\circ$, making the design well-suited for phase-sensitive radar and coherent communication systems.

A key contribution of this work lies in the transparent and application-relevant evaluation of power-handling capability. The rotary joint is experimentally validated for continuous-wave (CW) operation up to 2 kW, while moderate-duration pulsed operation up to 30 kW is assessed through particle-in-cell (PIC) simulations. This dual-level verification approach captures both thermally limited and field-limited operating regimes, providing a realistic assessment of the rotary joint's operational envelope. In contrast to short-duration high-power microwave (HPM) breakdown tests reported in the literature, which primarily characterize peak electric-field withstand capability, the adopted methodology reflects practical RF operating conditions encountered in real X-band front-end systems.

As summarized in Table 2, the proposed rotary joint outperforms existing X-, Ku-, and S-band designs by offering a balanced combination of low loss, ultra-low wobble, wide operational bandwidth, and validated high-power performance. This comprehensive performance profile distinguishes the proposed design from prior works that emphasize either wideband operation, compactness, or extreme peak power endurance in isolation.

In conclusion, the proposed rotary joint provides a robust and practically deployable solution for next-generation X-band radar and high-power satellite communication systems. The demonstrated electrical stability, power robustness, and measurement-backed verification make the design particularly attractive for applications requiring continuous rotation, high phase fidelity, and sustained high-power transmission. Future work will focus on extending the proposed architecture to multi-channel and multi-band rotary joint configurations, as well as experimental validation under long-term operational and environmental stress conditions.

REFERENCES

[1] Borisov, S. and A. Shishlov, "Antennas for SatCom-on-the-move, review," in *2014 International Conference on Engineering and Telecommunication*, 3–7, Moscow, Russia, 2014.

[2] Güvenç, M., I. Şişman, and A. A. Ergin, "Design, optimization and fabrication of a X-band septum polarizer for satellite communication," in *2023 IEEE International Symposium on Antennas and Propagation and USNC-URSI Radio Science Meeting (USNC-URSI)*, 1347–1348, Portland, OR, USA, 2023.

[3] Azim, M. T., J. Park, and S.-O. Park, "Contactless linear rotary joint at Ku-band," *IEEE Microwave and Wireless Components Letters*, Vol. 29, No. 6, 373–375, Jun. 2019.

[4] Yevdokymov, A., V. Kryzhanovskiy, V. Pazynin, and K. Sirenko, "Ka-band waveguide rotary joint," *IET Microwaves, Antennas & Propagation*, Vol. 7, No. 5, 365–369, Apr. 2013.

[5] Şişman, I., T. H. Ergin, D. E. Barkana, and H. A. Ülkü, "Design and realization of an X band monopulse feed antenna for low earth orbit (LEO) satellite ground station," *International Journal of Antennas and Propagation*, Vol. 2024, No. 1, 6659390, 2024.

[6] Ghosh, S. and L. C. Da Silva, "Waveguide rotary joint and mode transducer structure therefor," US Patent 5,442,329, Aug. 1995.

[7] Kaiden, M., K. Kimura, H. Ogawa, T. Kasuga, M. Tsuboi, and Y. Murata, "Septum polarizer for Ka-band H-shaped rotary joint," *Journal of Infrared, Millimeter, and Terahertz Waves*, Vol. 30, No. 7, 727–737, 2009.

[8] Chang, T. H. and B. R. Yu, "High-power millimeter-wave rotary joint," *Review of Scientific Instruments*, Vol. 80, No. 3, 034701, 2009.

[9] Abramov, V. I., H.-J. Park, D.-H. Kim, and T.-H. Lee, "U-style rotary joint with E/sub 01/mode for millimeter waves," in *2004 IEEE MTT-S International Microwave Symposium Digest (IEEE Cat. No.04CH37535)*, Vol. 3, 1879–1882, Fort Worth, TX, USA, 2004.

[10] Rambabu, K. and J. Bornemann, "Compact single-channel rotary joint using ridged waveguide sections for phase adjustment," *IEEE Transactions on Microwave Theory and Techniques*, Vol. 51, No. 8, 1982–1986, Aug. 2003.

[11] McNamara, D. A., D. A. McNamara, and L. T. Hildebrand, "Fullwave analysis of non-contacting rotary joint choke sections using the generalised scattering matrix (GSM) approach," *IEE Proceedings — Microwaves, Antennas and Propagation*, Vol. 150, No. 1, 5–10, 2003.

[12] Franco, M. A. R., V. A. Serrao, C. Fuhrmann, and S. B. Herdade, "A simple procedure for impedance matching and tuning of microwave couplers for an electron linear accelerator," *IEEE Transactions on Microwave Theory and Techniques*, Vol. 49, No. 3, 562–564, 2001.

[13] Yousefian, M., S. J. Hosseini, and M. Dahmardeh, "Compact broadband coaxial to rectangular waveguide transition," *Journal of Electromagnetic Waves and Applications*, Vol. 33, No. 9, 1239–1247, 2019.

[14] Smith, P. H. and G. H. Mongold, "A high power rotary waveguide joint," *IEEE Transactions on Microwave Theory and Techniques*, Vol. 12, No. 1, 55–58, 1964.

[15] King, H. E., "Broad-band coaxial choked coupling design," *IRE Transactions on Microwave Theory and Techniques*, Vol. 8, No. 2, 132–135, 1960.

[16] Liu, J., J. Shi, J. Qiu, H. Chen, and X. Wu, "Development of a high-power X-band compact RF rotary joint," *Nuclear Instruments and Methods in Physics Research Section A: Accelerators, Spectrometers, Detectors and Associated Equipment*, Vol. 908, 72–77, 2018.

[17] Azim, M. T., J. Park, L. Minz, R. S. Aziz, and S.-O. Park, "Single channel linear rotary joint at X-band," in *2018 International Symposium on Antennas and Propagation (ISAP)*, 1–2, Busan, Korea, 2018.

[18] Pandey, A., T. Singh, S. Doongarwal, and S. Choube, "Development of RF rotary joint for IFF RADAR application," in *2022 IEEE Microwaves, Antennas, and Propagation Conference (MAPCON)*, 1514–1517, Bangalore, India, 2022.

[19] Morini, A., "Design of a dual-band rotary joint operating in X- and Ka-bands," *IEEE Transactions on Microwave Theory and Techniques*, Vol. 59, No. 6, 1461–1467, Jun. 2011.

[20] Zhang, Z., K. Xue, and Z. Weng, "A high-power radar rotary joint," *Frontiers in Physics*, Vol. 10, 948570, 2022.

[21] Farahbakhsh, A., "Wideband rotary joint based on gap waveguide technology," *IEEE Transactions on Microwave Theory and Techniques*, Vol. 69, No. 10, 4385–4391, 2021.

[22] Pandey, A., T. Singh, and B. M. Jha, "Development of non-contacting type microwave rotary joint for S-band radar application," in *2024 Second International Conference on Microwave, Antenna and Communication (MAC)*, 1–4, Dehradun, India, 2024.